

INVERSE EQUIVALENT SURFACE CURRENT METHOD WITH HIERARCHICAL HIGHER ORDER BASIS FUNCTIONS, FULL PROBE CORRECTION AND MULTILEVEL FAST MULTIPOLE ACCELERATION (INVITED PAPER)

T. F. Eibert, Ismatullah, E. Kaliyaperumal, and C. H. Schmidt

Technische Universität München
Lehrstuhl für Hochfrequenztechnik
80290 Munich, Germany

Abstract—An inverse equivalent surface current method working with equivalent electric and/or magnetic surface current densities on appropriately chosen Huygens surfaces is investigated. The considered model with triangular surface meshes is compatible with the models known from method of moments (MoM) solutions of surface integral equations. Divergence conforming current basis functions of order 0.5 and of order 1.5 are considered, where the order 0.5 functions are the well-known Rao-Wilton-Glisson basis functions. Known near-field samples typically obtained from measurements are mapped on the unknown equivalent surface current densities utilizing the radiation integrals of the currents as forward operator, where the measurement probe influence is formulated in a MoM like weighting integral. The evaluation of the forward operator is accelerated by adaptation of the multilevel fast multipole method (MLFMM) to the inverse formulation, where the MLFMM representation is the key to full probe correction by employing only the far-field patterns of the measurement probe antennas. The resulting fully probe corrected algorithm is very flexible and efficient, where it is found that the computation speed is mostly dependent on the MLFMM configuration of the problem and not that much on the particular equivalent current expansion as long as the expansion is able to represent the currents sufficiently well. Inverse current and far-field pattern results are shown for a variety of problems, where near-field samples obtained from simulations as well as from realistic measurements are considered.

Received 16 June 2010, Accepted 22 July 2010, Scheduled 28 July 2010
Corresponding author: T. F. Eibert (eibert@tum.de).

1. INTRODUCTION

Various applications of practical interest, for example antenna diagnostics, near-field (NF) far-field (FF) transformation etc., require the investigation of radiated/scattered NFs, where these fields are known for a set of observation points located arbitrarily around the object under test. A variety of techniques, such as free-space eigenmode expansions for canonical surfaces [1–4] or Huygens equivalent electric/magnetic current representations [5–7], can be found in the literature. The inverse equivalent current methods (ECMs) usually expand the unknown surface current densities employing pulse or Rao-Wilton-Glisson (RWG) [8] basis functions, and obviously the ECMs have the potential to work with arbitrary Huygens surfaces and even with irregular sample locations. In order to achieve an efficient ECM, it is highly desirable to have an accelerated evaluation of the full radiation operators. Therefore, fast Fourier transform (FFT) based algorithms have been of very early interest [9]. The known disadvantage of the FFT approach is its restriction to planar Huygens and scan surfaces with regular sampling. More flexibility is achieved by the fast multipole method (FMM), where a single level FMM was applied with limited success in [10] to accelerate an ECM. Also, the algebraic adaptive cross approximation (ACA) technique has been implemented in order to compress the discretized forward IE operator in [11].

In a recent publication [7], a robust and efficient ECM has been reported by the application of the spherical harmonics expansion based MLFMM (SE-MLFMM) [12] with NF and FF translations [13,14] employed for the iterative solution of the normal equation system obtained from RWG based discretization of the ECM IE operator. In this method, an IE is formulated relating the discretized unknown equivalent surface current densities and known NF samples. The IE is solved by a method of moments (MoM) like solution procedure and the inverse equivalent currents are modeled using RWG basis functions, which are known to be of mixed order 0.5.

In MoM solutions of IEs, it is known that higher-order (HO) modeling of current densities often provides great reduction of the number of unknowns for a given problem and a desired accuracy or equivalently, better accuracies are achievable for the same number of basis functions, but of higher order (e.g., [15–17] etc.).

In the current contribution, hierarchical curl-conforming nearly-orthogonal HO expansion functions (up to mixed order 1.5) available in [16] have been transformed to the divergence-conforming counterparts for the discretization of inverse equivalent currents on

triangular meshes [17].

In most applications, the NF data of the antenna under test (AUT) is obtained from measurements, which are influenced by measuring probes. Therefore, a correction of the probe influence within the inverse solution algorithm is mandatory in order to obtain accurate results. In the present work, full probe correction capability is achieved by virtue of the MLFMM formulation adapted to the inverse solver, since the probe influence appears just as the FF pattern of the probe within the k -space integrals to be evaluated in the MLFMM [18].

In what follows, the inverse model and the formulation of the inverse constraint equations are first discussed. The essential contribution of the present paper is the MLFMM accelerated ECM formulation, which includes a full measurement probe correction, and the investigation of HO basis functions within the MLFMM accelerated ECM. The rigorous probe correction becomes possible due to the k -space representation within the MLFMM formulation. Also, a unified representation for NF and FF translations within the MLFMM is given. The iterative solution of the equation system is described and details on the implementation of the probe correction are given. The resulting algorithm provides full probe correction capability for arbitrary measurement sample distributions together with low computational cost and complexity. A variety of results are presented, where the behavior of the algorithm for various measurement probes, for different discretizations, and for different basis function orders is demonstrated. Results with synthesized NF measurement data obtained from simulations as well as with NF data from realistic measurements are considered. In particular, the functionality of the probe correction algorithm is demonstrated for badly miss-aligned halfwave dipoles, which produce a very complicated receiving pattern from the point of view of an NF measurement.

2. FORMULATION

2.1. Model and Constraint Equations

Consider an antenna or scatterer configuration as illustrated in Figs. 1(a) or (b), where the radiated or scattered electromagnetic NF is sampled by arbitrary measurement probes at some arbitrary sample locations \mathbf{r}_M . The measured signals at the output ports of the probes are characterized by the open-circuit voltages $U(\mathbf{r}_M)$, where time harmonic fields with $e^{j\omega t}$ are considered throughout this paper. The uniqueness of the introduced equivalent currents can be studied by invoking Huygens' and equivalence principles [19], where this is however not that important for the present study. Instead

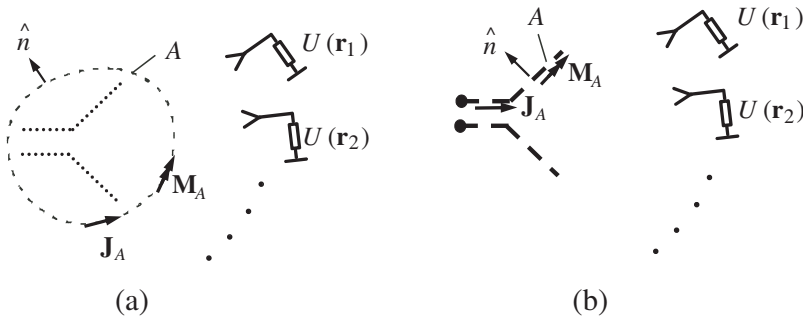


Figure 1. Inverse equivalent current model and near-field measurement configuration: (a) Closed Huygens surface around radiation or scattering object. (b) Equivalent currents directly located on the antenna or scatterer.

our models according to Figs. 1(a) or (b) can be chosen arbitrarily and we may end up with a unique or non unique description, which is typically solved in a least mean square error (LMSE) sense. In the case of Fig. 1(a), the closed surface can be placed as close to the object's surface as possible in order to obtain the maximum amount of diagnostic information or it can be chosen in some distance to the object, where the field distribution is smoother. The idea of models according to Fig. 1(b) is to introduce a priori information about the object's geometry and material composition, where in particular magnetic surface current densities are omitted on the surface of perfect electric conductors (PEC). The electric field intensity $\mathbf{E}(\mathbf{r})$ generated by the equivalent surface current densities $\mathbf{J}_A(\mathbf{r}')$ (electric) and $\mathbf{M}_A(\mathbf{r}')$ (magnetic) together with some incident field $\mathbf{E}^{inc}(\mathbf{r})$ is given by

$$\mathbf{E}(\mathbf{r}) = \iint_A \left[\bar{\mathbf{G}}_J^E(\mathbf{r}, \mathbf{r}') \cdot \mathbf{J}_A(\mathbf{r}') + \bar{\mathbf{G}}_M^E(\mathbf{r}, \mathbf{r}') \cdot \mathbf{M}_A(\mathbf{r}') \right] dA' + \mathbf{E}^{inc}(\mathbf{r}), \quad (1)$$

where $\bar{\mathbf{G}}_J^E(\mathbf{r}, \mathbf{r}')$ is the dyadic Green's function for electric currents and $\bar{\mathbf{G}}_M^E(\mathbf{r}, \mathbf{r}')$ is the dyadic Green's function for magnetic currents, both typically given in free space. Also, A is the surface on which the surface currents are presumed. Since the electric fields at the sample locations \mathbf{r}_M to be used in (1) are typically measured by a measurement probe with some finite dimensions and some direction dependence, the influence of this measurement probe must be considered and this can be done by working with the probe open-circuit voltage $U_m(\mathbf{r}_M)$

representing the measurement signal according to

$$U_m(\mathbf{r}_M) = \iiint_{V_{probe}} \mathbf{w}_m(\mathbf{r}) \cdot \mathbf{E}(\mathbf{r}) dV, \quad (2)$$

where V_{probe} is the volume of the probe supporting equivalent currents representing the probe influence and $\mathbf{w}_m(\mathbf{r})$ is the spatial vector weighting function of the probe representing the equivalent currents on the probe, including conversion to voltage. The index m indicates that various probes can be used at the different measurement locations, where typically two independent polarizations will be measured at every measurement location \mathbf{r}_M . In order to numerically solve the set of constraint equations resulting from the combination of (1) and (2), the surface current densities in (1) are discretized on triangular surface meshes according to

$$\mathbf{J}_A(\mathbf{r}') = \sum_p J_p \boldsymbol{\beta}_p(\mathbf{r}'), \quad \mathbf{M}_A(\mathbf{r}') = \sum_q M_q \boldsymbol{\beta}_q(\mathbf{r}'), \quad (3)$$

where $\boldsymbol{\beta}_{p,q}$ are hierarchical vector basis functions [17]. These basis functions are derived from the nearly orthogonal tangentially continuous field basis functions $\boldsymbol{\alpha}_{p,q}$ as presented in [16], which are converted into normally continuous current counterparts $\boldsymbol{\beta}_{p,q}$ using

$$\boldsymbol{\beta}_{p,q} = \hat{n}_{p,q} \times \boldsymbol{\alpha}_{p,q}, \quad (4)$$

where $\hat{n}_{p,q}$ are appropriately oriented unit surface normals on the discretization triangles. Since the implementation of the higher order basis functions within the ECM is very similar to the case of surface IE solutions by MoM, we refer to [15, 17] for further description of the basis functions incorporated in the present ECM formulation.

The resulting linear typically non-quadratic equation system is

$$\underbrace{\left\| \begin{array}{ccccc} \dots & \vdots & \dots & \vdots & \dots \\ \dots & C_{mp}^J & \dots & C_{mq}^M & \dots \\ \dots & \vdots & \dots & \vdots & \dots \end{array} \right\|}_{\|C\|} \underbrace{\left\{ \begin{array}{c} \vdots \\ j_p \\ \vdots \\ m_q \\ \vdots \end{array} \right\}}_{\{x\}} = \underbrace{\left(\begin{array}{c} \vdots \\ U_m(\mathbf{r}_M) - U_m^{inc}(\mathbf{r}_M) \\ \vdots \end{array} \right)}_{\{b\}} \quad (5)$$

where normalized current expansion coefficients $j_p = J_p/(c_2 J_0)$ and $m_q = M_q/(c_2 M_0)$ were introduced in order to have the flexibility to improve the conditioning of the resulting equation system. A well conditioned equation system is typically obtained by choosing J_0 and

M_0 according to $M_0/J_0 = Z_0 = \sqrt{\mu_0/\varepsilon_0} \approx 377 \Omega$, where either M_0 or J_0 can be chosen freely. c_2 is a further scaling factor, which can be used for a different scaling of the 2nd order functions within the hierarchical basis function set. Another way of normalization is, e.g., presented in [6]. $U_m^{inc}(\mathbf{r}_M)$ is calculated according to (2) with \mathbf{E} replaced by \mathbf{E}^{inc} . Also, the matrix entries are given by

$$C_{mp}^J = c_2 J_0 \iiint_{V_{probe}} \mathbf{w}_m(\mathbf{r}) \cdot \iint_A \bar{\mathbf{G}}_J^E(\mathbf{r}, \mathbf{r}') \cdot \boldsymbol{\beta}_p(\mathbf{r}') dA' dV, \quad (6)$$

$$C_{mq}^M = c_2 M_0 \iiint_{V_{probe}} \mathbf{w}_m(\mathbf{r}) \cdot \iint_A \bar{\mathbf{G}}_M^E(\mathbf{r}, \mathbf{r}') \cdot \boldsymbol{\beta}_q(\mathbf{r}') dA' dV. \quad (7)$$

The required Green's functions in free space are

$$\bar{\mathbf{G}}_J^E(\mathbf{r}, \mathbf{r}') = -j \frac{\omega \mu}{4\pi} \left(\bar{\mathbf{I}} + \frac{1}{k^2} \nabla \nabla \right) \frac{e^{-jk|\mathbf{r}-\mathbf{r}'|}}{|\mathbf{r}-\mathbf{r}'|}, \quad (8)$$

$$\bar{\mathbf{G}}_M^E(\mathbf{r}, \mathbf{r}') = -\frac{1}{4\pi} \nabla \times \bar{\mathbf{I}} \frac{e^{-jk|\mathbf{r}-\mathbf{r}'|}}{|\mathbf{r}-\mathbf{r}'|}. \quad (9)$$

Utilizing the FMM representation of the scalar Green's function of free space [20]

$$\frac{e^{-jk|\mathbf{X}+\mathbf{d}|}}{|\mathbf{X}+\mathbf{d}|} = \lim_{L \rightarrow \infty} \oint\!\!\!\!\!\oint e^{-j\mathbf{k} \cdot \mathbf{d}} T_L(\hat{k}, \hat{X}) d\hat{k}^2 \quad (10)$$

valid for arbitrary vectors with $|\mathbf{X}| > |\mathbf{d}|$ with the FMM translation operator

$$T_L(\hat{k}, \hat{X}) = \frac{jk}{4\pi} \sum_{l=0}^L (-j)^l (2l+1) h_l^{(2)}(k|\mathbf{X}|) P_l(\hat{k} \cdot \hat{X}), \quad (11)$$

where $h_l^{(2)}$ is the second kind spherical Hankel function of degree l and P_l is the Legendre polynomial of degree l , the FMM representation of the matrix entries in (6) and (7)

$$C_{mp}^J = -\frac{j\omega\mu c_2 J_0}{4\pi} \oint\!\!\!\!\!\oint T_L(\hat{k}, \hat{r}_{Mg}) \tilde{\mathbf{w}}_m^*(\hat{k}) \cdot (\bar{\mathbf{I}} - \hat{k}\hat{k}) \cdot \tilde{\boldsymbol{\beta}}_p(\hat{k}) d\hat{k}^2, \quad (12)$$

$$C_{mq}^M = -\frac{c_2 M_0}{4\pi} \oint\!\!\!\!\!\oint T_L(\hat{k}, \hat{r}_{Mg}) \tilde{\mathbf{w}}_m^*(\hat{k}) \cdot (\tilde{\boldsymbol{\beta}}_q(\hat{k}) \times \hat{k}) d\hat{k}^2 \quad (13)$$

is obtained. The \sim indicates Fourier transform according to

$$\tilde{\boldsymbol{\beta}}_{p,q}(\hat{k}) = \iint_A \boldsymbol{\beta}_{p,q}(\mathbf{r}') e^{j\mathbf{k} \cdot (\mathbf{r}' - \mathbf{r}_g)} dA', \quad (14)$$

where \mathbf{r}_g is the center of the FMM or MLFMM group [12, 20] to which basis function $\beta_{p,q}$ belongs and \hat{k} is the unit vector in the direction of \mathbf{k} . Similarly, $\tilde{\mathbf{w}}_m^*(\hat{k})$ is the inverse Fourier transform (conjugate complex indicated by the $*$) with respect to the measurement location \mathbf{r}_M (coordinate origin of the probe). \mathbf{r}_{Mg} in (12) and (13) is therefore $\mathbf{r}_{Mg} = \mathbf{r}_M - \mathbf{r}_g$. If $|\mathbf{r}_{Mg}|$ is considerably larger than the relevant MLFMM group dimensions and the extent of the probe antenna (i.e., some FF criterion is fulfilled) [13, 14], the translation operator in (11) can be replaced by

$$T^{FF}(\mathbf{r}_{Mg}) = \frac{e^{-jk|\mathbf{r}_{Mg}|}}{|\mathbf{r}_{Mg}|} \delta(\hat{k} - \hat{r}_{Mg}). \quad (15)$$

The Dirac- δ in this FF translation operator together with the integration over the Ewald sphere in (12) and (13) leads to the well-known FF representation of the matrix entries with one locally plane wave propagating along the vector from the source location to the observation location.

The matrix entries in (12) and (13) are written with direct translations from some MLFMM group center to probe positions. However, the evaluation can also be done in a way that the translations are performed into some MLFMM group center and the wave contributions at the probe positions are then obtained by the MLFMM typical disaggregation and anteprolation procedures [7, 12, 13, 20].

2.2. Solution of Equation System and Probe Correction

The linear equation system (5) is solved in an LMSE sense and this is equivalent to solving the normal equation [21, 22]

$$\|C\|^{ad} \|C\| \{x\} = \|C\|^{ad} \{b\}, \quad (16)$$

where $\|C\|^{ad}$ is the adjoint (transpose conjugate complex) of $\|C\|$. Further details on the solution of the equation system are found in [7]. Important to note is that an iterative equation solver is employed (based on the generalized minimal residual solver (GMRES)), which requires only the evaluation of matrix/vector products for solution. These matrix/vector products are very efficiently evaluated by using the MLFMM like strategy as introduced in [7], which combines NF and FF translations in a very efficient manner and which was extended in order to consider the probe receiving characteristics represented by $\tilde{\mathbf{w}}_m^*(\hat{k})$ in (12) and (13). These probe receiving characteristics are nothing else than the FF patterns of the weighting functions in standard FMM or MLFMM solutions of IEs. However, in the numerical implementation, transformations from the global coordinate system

into the local probe coordinate systems at the various measurement locations must be performed very carefully.

If the measurement location is very close to the sources, the calculation of the matrix entries according to (6) and (7) would be desirable. However, this would require the knowledge of appropriate spatial functions $\mathbf{w}_m(\mathbf{r})$. In order to avoid these spatial functions, the FMM groups on the finest level are typically chosen so small that all matrix entries can be computed according to (12) and (13). If this does not work, because the support of the basis functions is too large, the basis functions can be even subdivided by treating the quadrature samples on the basis functions separately and collect their plane wave contributions at the individual probes. Towards this, the full FMM translation operator (11) or for less accurate results even the FF translation operator (15) can be used. The latter would be equivalent to the probe pattern correction procedure as discussed in [23].

3. RESULTS

An important aspect for the application of the MLFMM accelerated ECM is an appropriate choice of the MLFMM parameters. A lot of information on this topic is found in the relevant MLFMM literature, e.g., [20] and contained references. For the probe corrected ECM, the number L of multipoles in the MLFMM is chosen according to Eq. (8) in [18] with $d_0 = 3, \dots, 5$, where d is chosen as the sum of the MLFMM box size containing the sources and of the MLFMM box size containing the measurement probe. On higher levels both box sizes are typically equal. However, on the lowest level it must be considered that the size of the probe antenna can be larger than the MLFMM box size. Also, the order P of the spherical harmonics according to [12] used to expand the FF patterns of the basis functions is chosen as $P = L/2$ in order to achieve high accuracy. An appropriate FF criterion for the selection of FF translations within the MLFMM has been derived in [14] and is also used in [13]. In order to achieve good ECM results it is however recommended to increase this FF distance by a factor of 2 to 3.

The first considered example is the parabolic reflector with Yagi feed as displayed in Fig. 2. The diameter of the dish is 400 mm and the operation frequency is chosen to be 4.0 GHz. The reflector is fed by a 6-element Yagi antenna and reference simulations of the configuration were performed by the IE solver from CST MWS. The resulting 3D radiation pattern is also shown in Fig. 2. Employing the IE solver from CST MWS complete NF measurement scenarios with realistic $\lambda/2$ -probe antennas were performed. Spherical measurements were considered with a radius of 1 m, 36 samples in ϑ -direction and

72 samples in φ -direction. In one scenario, the probes were oriented horizontally and vertically resulting in a perfect alignment with $\hat{\vartheta}$ and $\hat{\varphi}$ in all spherical measurement positions. In the second scenario, the horizontal and vertical probes were rotated by 45° as illustrated in Fig. 3. The figure shows the local probe coordinate system where the local x -axis is always directed towards the global coordinate origin and the local z -axis along $\hat{\vartheta}$. The ECM computations have been worked

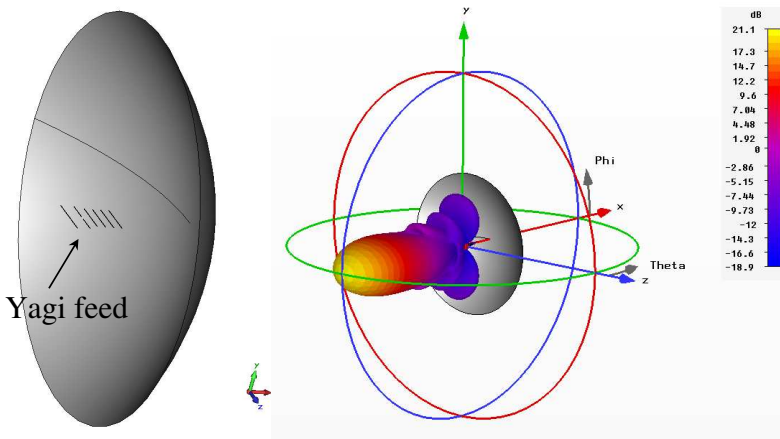


Figure 2. Geometry of Yagi-fed parabolic reflector together with 3D radiation pattern (gain, IEEE) from CST MWS.

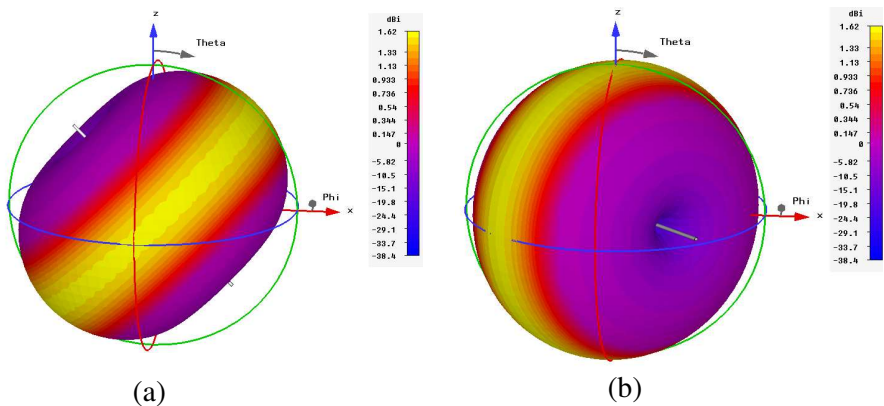


Figure 3. Orientation and radiation patterns (directivity) of the oblique $\lambda/2$ -probes obtained by rotation of 45° from the horizontal and vertical orientations, respectively.

out with a cuboidal Huygens surface ($390 \text{ mm} \times 390 \text{ mm} \times 115 \text{ mm}$) enclosing the reflector together with the feed supporting electric and magnetic surface current densities. Fig. 4 compares the ECM results for vertical and horizontal probes obtained for a mesh with a total of 38 610 (electric and magnetic) unknowns of order 0.5 with the reference results from CST MWS. Remarkable is that even the low cross polarized components show pretty good agreement. The computation time on one core of an Intel Core 2 Quad Q9550 CPU with 2.83 GHz was about 1 100 sec with a memory requirement of about 25 MByte. The radiation patterns for the case with oblique probe orientation

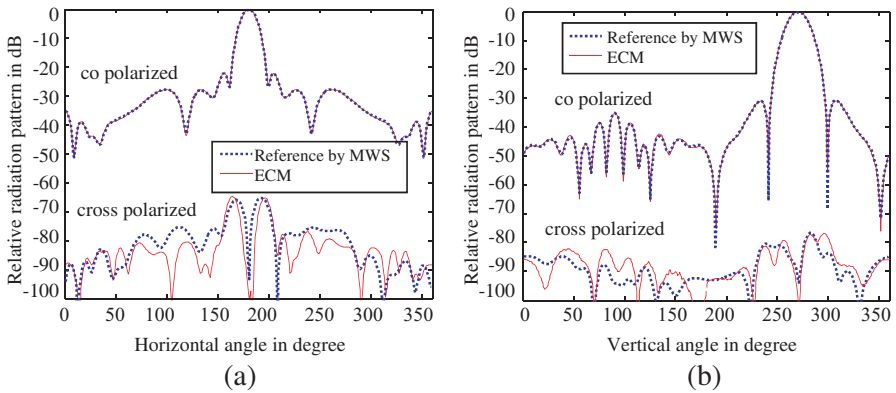


Figure 4. (a) E - and (b) H -plane radiation patterns obtained with vertical and horizontal $\lambda/2$ -dipole probes.

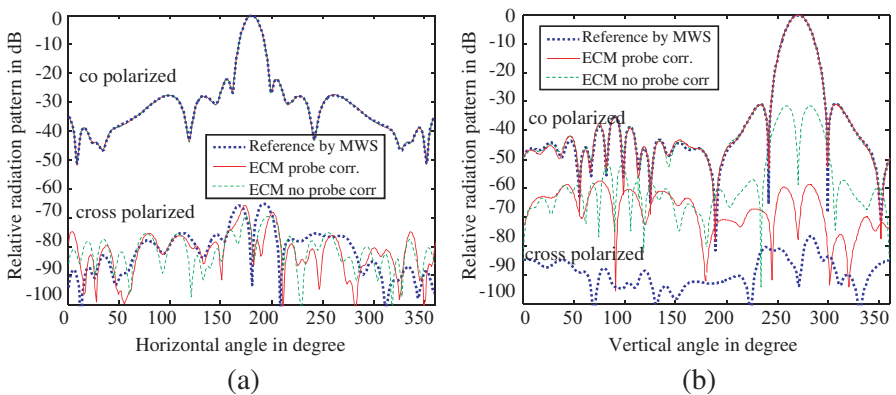


Figure 5. (a) E - and (b) H -plane radiation patterns obtained with the oblique $\lambda/2$ -dipoles probes, see Fig. 3.

are shown in Fig. 5. ECM results with probe correction and without probe correction are compared with the reference results from CST MWS. The ECM results without probe correction were computed with the radiation patterns of the horizontal and vertical probes instead of the patterns of the oblique probes. Both E -plane patterns compare very well with the reference, whereas the H -plane pattern shows some discrepancies in particular for the cross polarized component. However, from the E -plane pattern it can be seen, that the cross polarized component possesses a very deep null in the H -plane and that the observed error in the H -plane looks obviously much more dramatic than it is. Moreover, it is clearly seen, that the probe correction improves the value of the cross polarized component by about 30 dB. The achieved results with deliberately badly misaligned probes show that the presented probe correction works even for very complicated probes without appreciable symmetry.

In the next example, inverse ECM currents on a 20λ PEC plate are investigated, where only electric currents on the PEC plate are assumed. Firstly, the scattered electric fields on a spherical grid of 11 536 sample locations due to a plane wave incident on the plate at grazing angle have been computed employing MoM solution of IE with sufficiently fine triangular discretization of the plate. The influence of a possible measurement probe is not considered in this example and the ECM solution is directly obtained with ϑ - and φ -components of the

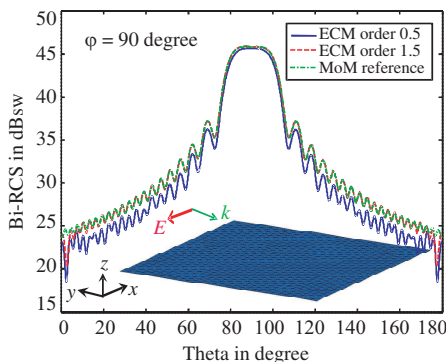


Figure 6. Bistatic radar cross section (RCS) in vertical plane ($\varphi = 90^\circ$) of a PEC plate with side length 20λ due to inverse equivalent currents (ECM) of order 0.5 and 1.5 on the surface of plate computed from 11 536 field samples on a sphere with radius 20 m. The field samples were computed by MoM with a plane wave at grazing incidence.

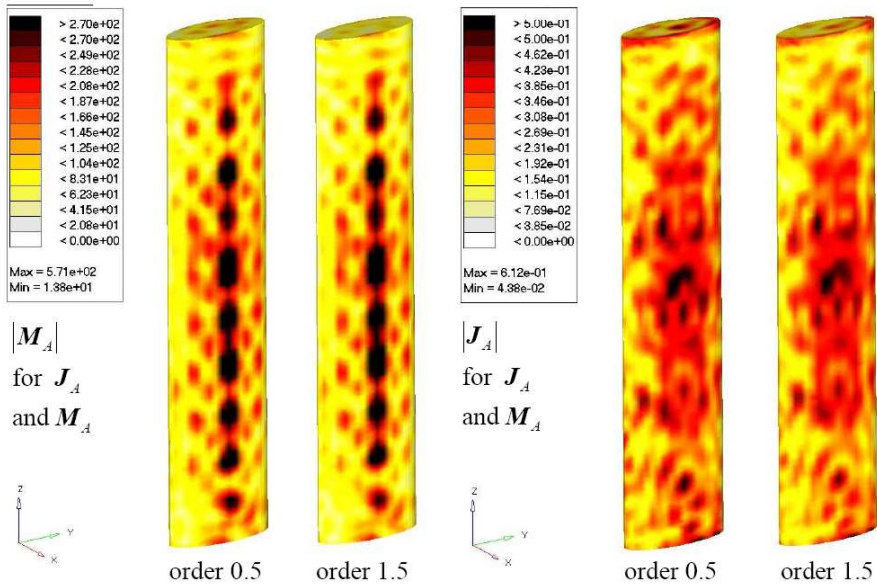


Figure 7. Equivalent surface current densities on a Huygens surface representing base station antenna Kathrein 742 445 radiating at 1.92 GHz. The Huygens surface is the surface of an elliptical cylinder of height 1 490 mm with half axes 157 mm and 60 mm. Electric and magnetic surface currents were assumed in the computations and lower order and higher order results are compared.

electric field. From the field samples, the ECM currents are computed on the plate with basis functions of order 0.5 and 1.5 using about 1.4 subdivisions per wavelength. For the solution of 2 727 order 0.5 unknowns and 9 170 order 1.5 unknowns, the ECM solver converged to less than 10^{-4} residual error in 6748 sec and 1180 sec (one core of Intel Core 2 Quad Q9550 CPU with 2.83 GHz), respectively. The computation time for the order 0.5 unknowns was very long for this example, since the approximation of the current distribution was below an acceptable limit and the ECM solver converged thus very badly. The memory requirements for order 0.5 and order 1.5 cases were 265 MByte and 272 MByte, respectively. The bistatic RCS in the vertical plane is plotted in Fig. 6. The order 1.5 results show better agreement with the MoM reference than those of order 0.5, even though the mesh was very coarse.

Finally, the realistic spherical NF measurement of a Kathrein 742 445 base station antenna at a frequency of 1.92 GHz is considered.

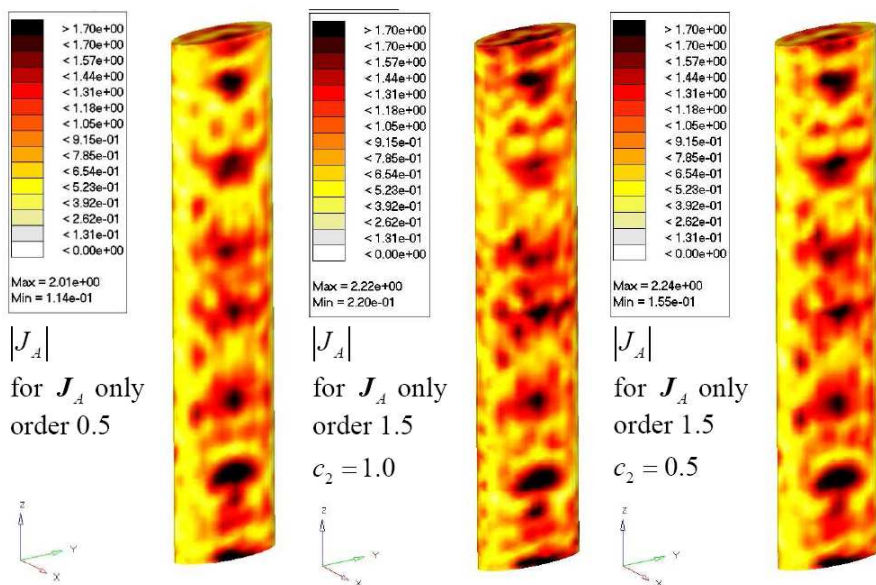


Figure 8. Equivalent surface current densities on a Huygens surface representing base station antenna Kathrein 742 445 radiating at 1.92 GHz. The Huygens surface is the surface of an elliptical cylinder of height 1 490 mm with half axes 157 mm and 60 mm. Electric surface currents were assumed in the computations and lower order and higher order results are compared with different values of second order scaling constant c_2 .

The number of NF measurement locations was 4 186, where two polarizations with open-ended hollow waveguide probes were measured. The ECM computations were performed with a closed Huygens surface as illustrated and described in Fig. 7, where different discretization densities and the available two different orders of basis functions were considered. Also, all computations were carried out with full probe correction. The current densities displayed in Figs. 7 and 8 were obtained with a relatively dense mesh with 9 008 triangles resulting in 13 512 basis function of order 0.5 and 45 040 basis functions of order 1.5 for every type of current. The order 1.5 computation with electric and magnetic currents comprised therefore a total of 90 080 basis functions. Fig. 7 shows both current types for the ECM computations assuming electric and magnetic currents with $Z_0 = 377 \Omega$ and $c_2 = 1.0$ (see (6) and (7) and discussion just before). As expected, due to the fine mesh the currents for the

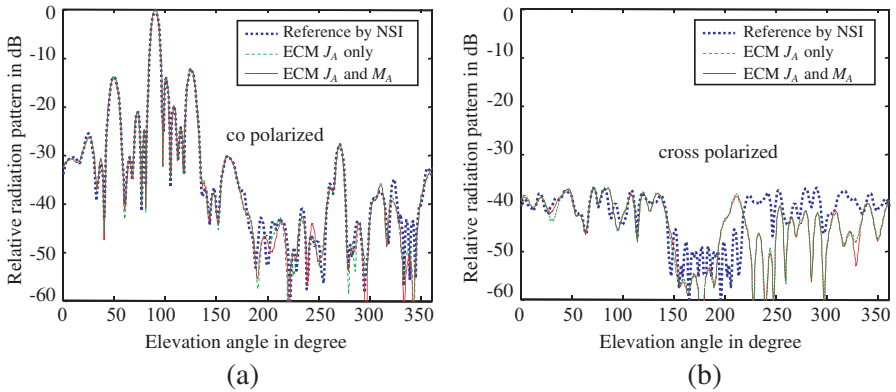


Figure 9. E -plane radiation patterns.

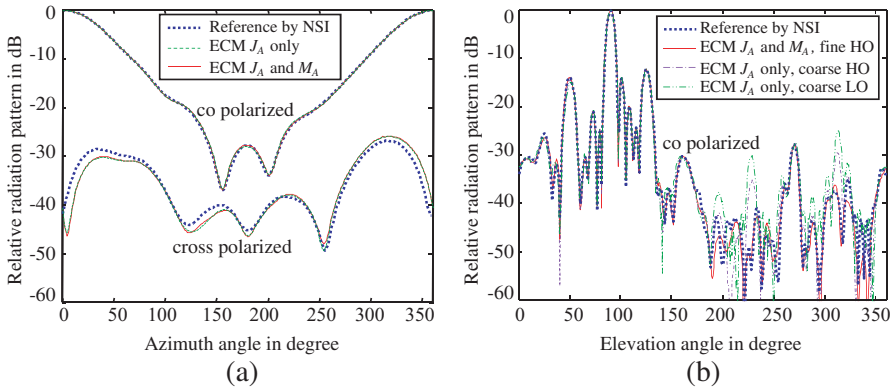


Figure 10. (a) H -plane radiation patterns, (b) E -plane radiation patterns for various meshes.

different expansion orders are very similar. The current distributions for the electric currents only case in Fig. 8 show some more differences, where the higher order currents appear more irregular than the lower order currents. An explanation for this behavior is that the equation system with the HO functions is usually worse conditioned than with the LO functions and regularization of this equation system by the iterative LMSE solver does not work that well. The conditioning of the equation system can be modified by the scaling parameter c_2 for the HO functions and it can be seen in Fig. 8 that $c_2 = 0.5$ reduces the irregularity of the current distribution compared to the case of $c_2 = 1$. The computation times for this mesh were on the order of

2000 sec to 4000 sec dependent on the chosen MLFMM parameters. It is interesting to note that the computation times with basis functions of order 0.5 and of order 1.5 were almost identical. Also, further computations with coarser meshes showed that the computation times are mostly determined by the MLFMM configuration, i.e., the grouping structure, the number of multipoles, etc. Since in the ECM all interactions are computed via MLFMM translations, the particular expansion with basis functions is no longer important after the field contributions of the basis functions have been aggregated in the MLFMM groups. In contrast to this, the memory requirement depends more on the number of basis functions. The computations with the 90080 order 1.5 unknowns required about 400 MByte of memory, whereas the computation with the 27024 order 0.5 unknowns required about 85 MByte. In both cases, the computations were carried out with a finest MLFMM group size of $(0.04 \text{ m})^3$ with multipole orders $L = 8$ and $P = 4$, where only NF MLFMM translations have been used. Fig. 9 shows the E -plane radiation patterns obtained with the fine mesh with 9008 triangles, where results for electric and magnetic currents as well as for electric currents only are shown. Both show very good agreement with the reference pattern even for the cross polarized component. Fig. 10(a) shows the corresponding H -plane patterns also with very satisfying agreement. Fig. 10(b) shows again E -plane patterns, but with different meshes and orders of basis functions. The fine HO (order 1.5) result is the same as shown in Fig. 9(a) and the coarse results were achieved with a mesh consisting of 1510 triangles with an average edge length of 4.2 cm. Electric current only computations are considered and order 0.5 and order 1.5 resulted in 2265 and 15100 basis functions, respectively. The radiation patterns show that the accuracy starts to deteriorate with this coarse mesh density, particularly with the lower order basis functions.

4. CONCLUSION

An inverse equivalent current method (ECM) has been studied for the reconstruction of equivalent surface currents on arbitrarily shaped radiation and scattering structures and in particular for the subsequent far-field radiation pattern and radar cross section computation. Higher-order basis functions of order 1.5 have been utilized to discretize the unknown inverse equivalent surface currents to obtain better accuracies with fewer discretizations per wavelength. Furthermore, the influence of the measurement probe on the near-field samples was compensated by a full probe correction technique without increasing the complexity of the algorithm. The full probe correction is

coming along with the plane wave representation of the multilevel fast multipole method (MLFMM), which was adapted in order to accelerate the forward operator and its adjoint computation within the inverse method. A variety of results has been presented proving the feasibility of the full probe correction, the MLFMM like acceleration, and the use of higher order basis functions. However, it was found that an MLFMM accelerated ECM is rather insensitive to the particular discretization since after aggregation of the radiated fields of the basis functions in the MLFMM groups the possible redundancy of an inefficient discretization is removed and all necessary interactions are computed after removing this redundancy. The presented algorithm is an efficient tool for diagnostic purposes, for the construction of equivalent sources representations, and for near-field far-field transformations.

ACKNOWLEDGMENT

The authors thank the “Deutsche Forschungsgemeinschaft (DFG)” for financial support of this work under grant EI 352/5-1. Also, the authors are grateful to KATHREIN-Werke KG, Rosenheim, Germany for providing the near-field measurement data as well as the NSI transformed far-field patterns in Section 3.

REFERENCES

1. Yaghjian, A., “An overview of near-field antenna measurements,” *IEEE Trans. Antennas Propag.*, Vol. 34, No. 1, 30–45, 1986.
2. Hansen, J. E., *Spherical Near-field Antenna Measurements*, IEE Electromagnetic Wave Series 26, 1988.
3. Kerns, D. M., “Plane-wave scattering-matrix theory of antennas and antenna-antenna interactions,” *National Bureau of Standards, Boulder CO*, 1981.
4. Cappellin, C., O. Breinbjerg, and A. Frandsen, “Properties of the transformation from the spherical wave expansion to the plane wave expansion,” *Radio Sci.*, Vol. 43, No. 1, 2008.
5. Sarkar, T. and A. Taaghoul, “Near-field to near/far-field transformation for arbitrary near-field geometry utilizing an equivalent electric current and MoM,” *IEEE Trans. Antennas Propag.*, Vol. 47, No. 3, 566–573, 1999.
6. Alvarez, Y., F. Las-Heras, and M. R. Pino, “Reconstruction of equivalent currents distribution over arbitrary three-dimensional surfaces based on integral equation algorithms,” *IEEE Trans. Antennas Propag.*, Vol. 55, No. 12, 3460–3468, 2007.

7. Eibert, T. F. and C. H. Schmidt, "Multilevel fast multipole accelerated inverse equivalent current method employing Rao-Wilton-Glisson discretization of electric and magnetic surface currents," *IEEE Trans. Antennas Propag.*, Vol. 57, No. 4, 1178–1185, 2009.
8. Rao, S. M., D. R. Wilton, and A. W. Glisson, "Electromagnetic scattering by surfaces of arbitrary shape," *IEEE Trans. Antennas Propag.*, Vol. 30, No. 3, 409–418, 1982.
9. Petre, P. and T. K. Sarkar, "Planar near-field to far-field transformation using an equivalent magnetic current approach," *IEEE Trans. Antennas Propag.*, Vol. 40, No. 11, 1348–1356, 1992.
10. Alvarez, Y., F. Las-Heras, M. R. Pino, and J. A. Lopez, "Acceleration of the sources reconstruction method via the fast multipole method," *IEEE Antennas Propag. Intern. Symp.*, 2008.
11. Lopez, Y. A., F. Las-Heras, and M. R. Pino, "Application of the adaptive cross approximation algorithm to the sources reconstruction method," *European Conf. Antennas Propag.*, 2009.
12. Eibert, T. F., "A diagonalized multilevel fast multipole method with spherical harmonics expansion of the k -space integrals," *IEEE Trans. Antennas Propag.*, Vol. 53, No. 2, 814–817, 2005.
13. Tzoulis, A. and T. F. Eibert, "Efficient electromagnetic near-field computation by the multilevel fast multipole method employing mixed near-field/far-field translations," *IEEE Antennas Wireless Propag. Lett.*, Vol. 4, 449–452, 2005.
14. Chew, W. C., T. J. Cui, and J. M. Song, "A FAFMA-MLFMA algorithm for electromagnetic scattering," *IEEE Trans. Antennas Propag.*, Vol. 50, No. 11, 1641–1649, 2002.
15. Jørgensen, E., J. L. Volakis, P. Meincke, and O. Breinbjerg, "Higher order hierarchical Legendre basis functions for electromagnetic modeling," *IEEE Trans. Antennas Propag.*, Vol. 52, No. 11, 2985–2995, 2004.
16. Sun, D. K., J. F. Lee, and Z. Cendes, "Construction of nearly orthogonal Nedelec bases for rapid convergence with multilevel preconditioned solvers," *SIAM J. Sci. Comput.*, Vol. 23, No. 4, 1053–1076, 2001.
17. Ismatullah and T. F. Eibert, "Surface integral equation solutions by hierarchical vector basis functions and spherical harmonics based multilevel fast multipole method," *IEEE Trans. Antennas Propag.*, Vol. 57, No. 7, 2084–2093, 2009.
18. Schmidt, C. H., M. M. Leibfritz, and T. F. Eibert, "Fully probe-corrected near-field far-field transformation employing plane

- wave expansion and diagonal translation operators,” *IEEE Trans. Antennas Propag.*, Vol. 56, No. 3, 737–746, 2008.
19. Araque Quijano, J. L. and G. Vecchi, “Field and source equivalence in source reconstruction on 3D surfaces,” *Progress In Electromagnetics Research*, Vol. 103, 67–100, 2010.
 20. Chew, W. C., J.-M. Jin, and E. Michielssen, *Fast and Efficient Algorithms in Computational Electromagnetics*, Artech House, Boston, 2001.
 21. Saad, Y., *Iterative Methods for Sparse Linear Systems*, PWS, Boston, 1996.
 22. Björck, A., *Numerical Methods for Least Squares Problems*, SIAM, Philadelphia, 1996.
 23. Las-Heras, F., B. Galocha, and J. L. Besada, “Equivalent source modelling and reconstruction for antenna measurement and synthesis,” *IEEE Antennas Propag. Intern. Symp.*, 2007.